Remote Sens. **2012**, *4*, 2314-2328; doi:10.3390/rs4082314

OPEN ACCESS

Remote Sensing

ISSN 2072-4292

www.mdpi.com/journal/remotesensing

Article

Polarimetric Decomposition Analysis of ALOS PALSAR Observation Data before and after a Landslide Event

Chinatsu Yonezawa [1,*], Manabu Watanabe [2] and Genya Saito [3]

[1] Graduate School of Agricultural Science, Tohoku University, 1-1 Amamiya-machi, Tsutsumidori, Aoba-ku, Sendai, Miyagi 981-8555, Japan

[2] Earth Observation Research Center, Japan Aerospace Exploration Agency, Tsukuba 305-8505, Japan; E-Mail: watanabe.manabu@jaxa.jp

[3] Tokyo Institute of Technology, Yokohama 226-8502, Japan; E-Mail: saito.g.aa@m.titech.ac.jp

***** Author to whom correspondence should be addressed; E-Mail: chinatsu@bios.tohoku.ac.jp; Tel.: +81-22-717-8661; Fax: +81-22-717-9542.

Received: 15 June 2012; in revised form: 30 July 2012 / Accepted: 30 July 2012 / Published: 7 August 2012

Abstract: Radar scattering mechanisms over landslide areas were studied using representative full polarimetric parameters: Freeman–Durden decomposition, and eigenvalue–eigenvector decomposition. Full polarimetric ALOS (Advanced Land Observation Satellite) PALSAR (Phased Array type L-band Synthetic Aperture Radar) datasets were used to examine landslides caused by the 2008 Iwate-Miyagi Nairiku Earthquake in northern Japan. The Freeman–Durden decomposition indicates that areas affected by large-scale landslides show dominance of the surface scattering component in both ascending and descending orbit data. The polarimetric parameters of eigenvalue–eigenvector decomposition, such as entropy, anisotropy, and alpha angle, were also computed over the landslide areas. Unsupervised classification based on the H-$\bar{\alpha}$ plane explicitly distinguishes landslide areas from others such as forest, water, and snow-covered areas, but does not perform well for farmland. A landslide area is difficult to recognize from a single-polarization image, whereas it is clearly extracted on the full polarimetric data obtained after the earthquake. From these results, we conclude that 30-m resolution full polarimetric data are more useful than 10-m resolution single-polarization PALSAR data in classifying land coverage, and are better suited to detect landslide areas. Additional information, such as pre-landslide imagery, is needed to distinguish landslide areas from farmland or bare soil.

Keywords: polarimetric SAR; scattering component disaster monitoring; earthquake; landslide

1. Introduction

SAR (Synthetic Aperture Radar) is capable of observing the Earth's surface in all weather conditions, day and night. Full polarimetric SAR data provide a scattering matrix of a terrain's surface. The scattering matrix consists of magnitude and phase at four polarizations, HH, HV, VH, and VV, that are sent and receive horizontally (H)- and vertically (V)-polarized waves by radar antenna [1]. Some methods have been suggested in order to obtain earth surface characteristics from full polarimetric data. Eigenvector decompositions of a coherency or covariance matrix were proposed by Cloude and Pottier [2]. An approach to the three-component scattering mechanism model was presented by Freeman and Durden [3], and a four-component approach was presented by Yamaguchi *et al.* [4]. These and other decomposition methods were reviewed [5]. The usefulness of full polarimetric SAR data for land cover classification was examined by Alberga *et al.* [6], and some of the techniques were applied to disaster monitoring- and assessment applications. A landslide caused by the 1999 Chi-chi earthquake in Taiwan was recognized using L-band airborne SAR data acquired after the disaster, and the characteristics of radar scattering mechanism were examined. The extent of the landslide was identified using data such as scattering entropy and anisotropy [7,8]. Other airborne L-band SAR data with full polarimetry were analyzed by Watanabe *et al.* [9] to detect a landslide area in Japan using three- and four-component decomposition techniques. It was shown that the landslide areas could be effectively identified on the basis of the dominance of the surface scattering component of the three-component scattering model.

The Iwate-Miyagi Nairiku earthquake (magnitude 7.2) struck an inland area of northern Honshu, the main island of Japan, on 14 June 2008, causing large landslides within mountainous forest areas. Several large landslides locally transformed forest to bare surface areas. Watanabe *et al.* [10] analyzed full polarimetric data obtained from ALOS (Advanced Land Observation Satellite) data after the earthquake, and showed that the landslide areas were well detected by combining the surface scattering and backscattering coefficients in VH polarization (σ^0_{VH}). ALOS carries an L-band (23.5-cm wavelength) SAR, termed PALSAR (Phased Array type L-band Synthetic Aperture Radar). PALSAR is the first space-borne SAR to have full polarizations mode. It also has three different polarimetric observation modes: single polarization (mainly HH), dual polarization (mainly HH and HV), and full polarization. Its range resolutions are 7–44, 14–88 and 24–89 m, respectively. In this paper, we used PALSAR full polarimetric data, acquired in both ascending and descending orbits before and after the earthquake-induced landslide. The pre- and post-landslide data used the same observation mode (off-nadir angle, flight direction). Since relatively few global-scale observations have been carried out by air-borne SAR, acquiring the data before the disaster with the same observation mode was hardly achievable for a landslide area observation. We adopted two representative full polarimetric decomposition models: a physically-based Freeman–Durden decomposition model, and a mathematically-strict eigenvalue–eigenvector decomposition model. These models are applied not

only to the landslide areas, but also to whole scenes, including forest, water surface and snow-covered areas, and areas of farmland or bare soil. Furthermore, results from the full polarimetric analysis were compared with those for single polarization. The comprehensive analysis results for landslide and neighboring areas are presented to clarify the radar scattering characteristics over the landslide areas by comparing other categories from the "actual" data, and to assist the identification of landslide areas from the pre- and post-event data.

2. Study Area and Data

2.1. Study Area

The epicenter of the Iwate-Miyagi Nairiku earthquake is located in the southern, inland part of Iwate Prefecture, at latitude 39 °1.7′N and longitude 140 °52.8′E (Figure 1).

Figure 1. Northern part of Honshu Island, Japan, with earthquake epicenter of the Iwate-Miyagi Nairiku earthquake (cross) and Mt. Kurikoma (square). Blank squares show observation areas of ALOS (Advanced Land Observation Satellite) PALSAR (Phased Array type L-band Synthetic Aperture Radar) full polarimetric mode. "Asc." orbit data was obtained on 4 June 2009. Observation dates of "Desc." orbits were 19 May 2006, 24 August 2008, 9 October 2008, and 24 November 2008. Shaded square corresponds with the area shown in Figure 2.

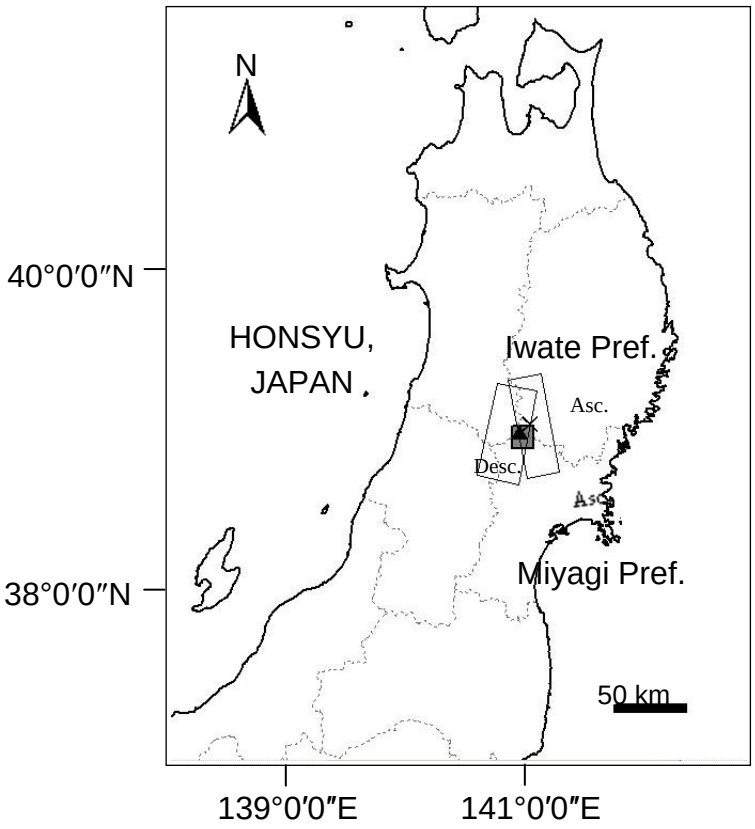

Seismic intensity, measured by the Japan Meteorological Agency, was 6-plus in Oushu City, Iwate Prefecture; and Kurihara City, Miyagi Prefecture. Seventeen people were killed and six were missing following the earthquake; almost all of the victims (21 persons) were killed by sediment disasters

caused by the earthquake [11]. The landslide areas were distributed in valleys adjacent to a mountainous area. At 1,627 m, Mt. Kurikoma is the highest peak in the disaster zone. The top of the mountain is covered by a snowcap from fall to spring.

Figure 2. ALOS AVNIR-2 (optical sensor, Advanced Visible and Near-infrared Radiometer type 2) false-color composite (Bands 4, 3, 2 in red, green and blue, respectively) obtained on 2 July 2008 after the 14 June 2008 earthquake. The white rectangle corresponds to the area shown in Figure 3.

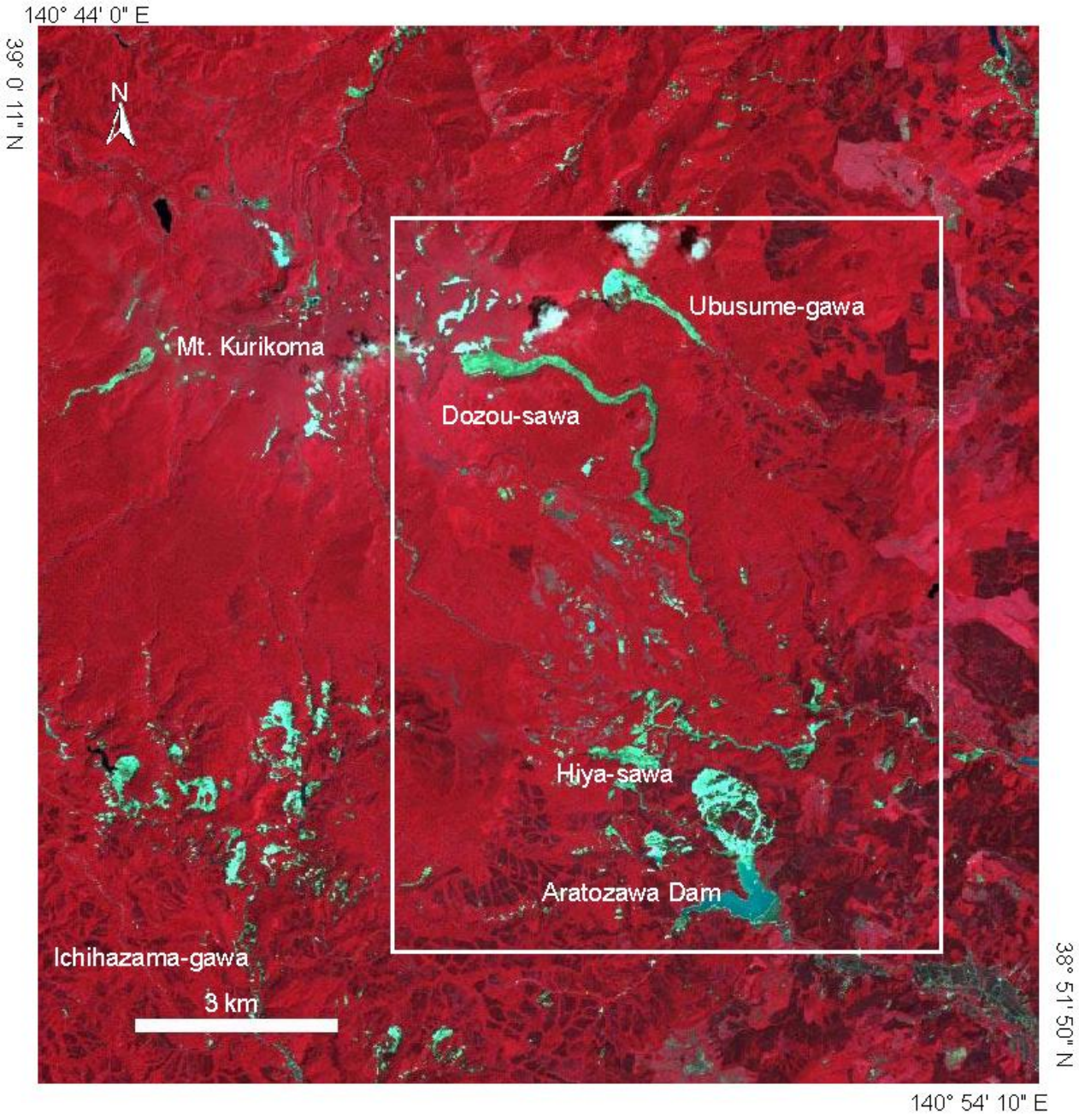

After the earthquake, many aerial photographs and much satellite data were obtained. Figure 2 shows the affected areas observed by ALOS AVNIR-2 (optical sensor, Advanced Visible and Near-infrared Radiometer type 2) on 2 July 2008. Figure 2 is a false-color composite image with landslides recognizable from the bare surfaces characterized by blue-green color. We use this image as a reference

for land coverage. The areas of earthquake damage are plotted on a damage status map [12,13]. The damage status map was generated from visual interpretation of aerial photographs obtained on 15, 16 and 18 June with 0.4 m ground resolution by the Geospatial Information Authority of Japan (GSI); and 16 and 18 June by Asia Air Survey Co., Ltd. GSI also conducted a field survey on 17 and 18 June. The affected regions were previously covered by forest and some farmland. Three major landslide event areas were selected and analyzed during this time. One of the largest landslide areas is located at the upstream end of the Aratozawa Dam reservoir. The affected area measured 900 × 1,300 m, and the displaced soil mass was estimated as 70 million m^3 by ground survey. A mudslide at Dozou-sawa, on the eastern slope of Mt. Kurikoma, was analyzed, and its soil mass by slope failure was estimated as 1 million m^3 by aerial photography [13]. The third landslide event area is Ubasume-gawa, where the area is 400 × 300 m [14], and soil mass by slope failure is estimated as 5 million m^3. Field observations were carried out on 23 August 2008 at Aratozawa Dam reservoir. Several photos were taken, and we observed that fallen trees were mixed in some parts of the landslide area.

2.2. PALSAR Data

PALSAR data of the disaster area were acquired via different observation modes. Many observations have been carried out in single- and dual-polarization modes. Full polarimetric datasets, including the epicenter before the earthquake, were acquired on 19 May 2006 in descending orbit. Those after the earthquake were observed on 24 August 2008, 9 October 2008, and 24 November 2008 in descending orbit; and on 4 June 2009 in ascending orbit. The off-nadir angle of 4 June 2009 data was 23.1°, and that of the other data was 21.5°. The observation areas are shown in Figure 1, and the datasets are summarized in Table 1.

Table 1. Summary of Observation Mode for PALSAR (Phased Array type L-band Synthetic Aperture Radar) Data.

Observation Mode	Before Disaster			After Disaster		
	Flight Direction	Observation Date	Off-nadir Angle (°)	Flight Direction	Observation Date	Off-nadir Angle (°)
Full polarimety	Desc.	19 May 2006	21.5	Desc.	24 August 2008	21.5
				Desc.	9 October 2008	21.5
				Desc.	24 November 2008	21.5
				Asc.	4 June 2009	23.1
Single polarimetry	Asc.	23 March 2008	34.3	Asc.	23 June 2008	34.3

3. Data Analysis

The polarimetric data were analyzed using PolSARpro software [15]. A Lee filter [16] was applied with a window size of 3 × 3 pixels, to reduce speckle noise to Level 1.1 PALSAR data, and was converted to the coherency matrix. We attempted a three-component polarimetric decomposition model [3] for full polarimetric data analysis. This model describes the scattering contributions from double-bounce, volume, and surface scattering by phase and intensity information in the polarimetric SAR data, as indicated below.

$$\begin{aligned}
\left\langle |S_{\mathrm{HH}}|^2 \right\rangle &= f_s|\beta|^2 + f_d|\alpha|^2 + f_v \\
\left\langle |S_{\mathrm{VV}}|^2 \right\rangle &= f_s + f_d + f_v \\
\left\langle S_{\mathrm{HH}} S_{\mathrm{VV}}^* \right\rangle &= f_s\beta + f_d\alpha + f_v/3 \\
\left\langle |S_{\mathrm{HV}}|^2 \right\rangle &= f_v/3 \\
\left\langle S_{\mathrm{HH}} S_{\mathrm{HV}}^* \right\rangle &= \left\langle S_{\mathrm{HV}} S_{\mathrm{VV}}^* \right\rangle = 0
\end{aligned} \tag{1}$$

Here, *Sij* is the scattering coefficient, transmitted in the *j* polarization plane, and received in the *i* polarization plane; and f_v, f_d, and f_s are the contribution to the power in VV polarization from volume, dihedral, and surface scattering. Parameters α and β are related to double-bounce and surface scattering. Determining whether double-bounce or surface scattering is the dominant contribution by using the sign of $Re(S_{HH}S^*_{VV})$ [17] enables us to identify the contribution of each scattering mechanism solely from SAR polarization data, without any field data.

We also attempted eigenvalue analysis of the coherency matrix. An eigenvalue–eigenvector decomposition was performed and scattering entropy *H*, polarimetric anisotropy *A*, and scattering mechanism parameter $\bar{\alpha}$ (alpha) were computed; unsupervised classification based on the *H*-$\bar{\alpha}$ plane [2] was attempted. *H*-*A*-$\bar{\alpha}$ parameters were independently defined. The elements of the scattering matrix are defined as

$$[S] = \begin{bmatrix} S_{HH} & S_{HV} \\ S_{VH} & S_{VV} \end{bmatrix} \tag{2}$$

The coherency matrix is defined as follows:

$$\begin{aligned}
\langle |T| \rangle &= \frac{1}{2} \begin{bmatrix} \left\langle |S_{HH} + S_{VV}|^2 \right\rangle & \left\langle (S_{HH} + S_{VV})(S_{HH} - S_{VV})^* \right\rangle & \left\langle 2S^*_{HV}(S_{HH} + S_{VV}) \right\rangle \\ \left\langle (S_{HH} - S_{VV})(S_{HH} + S_{VV})^* \right\rangle & \left\langle |S_{HH} - S_{VV}|^2 \right\rangle & \left\langle 2S^*_{HV}(S_{HH} - S_{VV}) \right\rangle \\ \left\langle 2S_{HV}(S_{HH} + S_{VV})^* \right\rangle & \left\langle 2S_{HV}(S_{HH} - S_{VV})^* \right\rangle & \left\langle 4|S_{HV}|^2 \right\rangle \end{bmatrix} \\
&= [U_3] \begin{bmatrix} \lambda_1 & 0 & 0 \\ 0 & \lambda_2 & 0 \\ 0 & 0 & \lambda_3 \end{bmatrix} [U_3]^\dagger
\end{aligned} \tag{3}$$

Parameters λ_1, λ_2, and λ_3 are calculated eigenvalues of [*T*], conventionally ordered such that $0 \le \lambda_3 \le \lambda_2 \le \lambda_1$.

Matrix [U_3] is parameterized as:

$$[U_3] = \begin{bmatrix} \cos\alpha_1 & \cos\alpha_2 & \cos\alpha_3 \\ \sin\alpha_1 \cos\beta_1 e^{j\delta_1} & \sin\alpha_2 \cos\beta_2 e^{j\delta_2} & \sin\alpha_2 \cos\beta_2 e^{j\delta_3} \\ \sin\alpha_1 \cos\beta_1 e^{j\gamma_1} & \sin\alpha_2 \cos\beta_2 e^{j\gamma_2} & \sin\alpha_3 \cos\beta_3 e^{j\gamma_3} \end{bmatrix} \tag{4}$$

Parameter α_i is directly related to the angle of incidence and dielectric constant of the surface with *i* ranging from 1 to 3. The β_i angles can be interpreted as orientation angles. γ_i and δ_i account for the phase relations.

The appearance probability of each λ_i contribution is given by

$$P_i = \frac{\lambda_i}{\sum_{j=1}^{3} \lambda_j} \tag{5}$$

The polarimetric scattering entropy is defined as follows:

$$H = \sum_{i=1}^{3} - P_i \log_3 P_i \quad 0 \le H \le 1 \tag{6}$$

,

The randomness of the scattering process is measured by entropy.

The dominant scattering mechanism for each pixel is given by the $\bar{\alpha}$ (alpha).

$$\overline{\alpha} = \sum_{i=1}^{3} P_i \alpha_i \quad 0 \le \overline{\alpha} \le 90 \tag{7}$$

,

Angle $\bar{\alpha}$ is associated with the type of scattering mechanism, and yields direct information about the scattering mechanism represented by each eigenvector. Consider a scattering matrix

$$[S] = \begin{bmatrix} a & 0 \\ 0 & b \end{bmatrix} \tag{8}$$

or rotated by θ. In case of $a = b$, which corresponds to surface scattering, the alpha parameter is 0. In case of $a = -b$, which corresponds to dihedral scattering, the alpha, parameter is $\pi/2$. In case of $a >> b$, which corresponds to highly anisotropic or dipole scattering, the alpha parameter is $\pi/4$. The other is in between them.

Polarimetric anisotropy, A, is defined as follows:

$$A = \frac{\lambda_2 - \lambda_3}{\lambda_2 + \lambda_3} \quad 0 \le A \le 1 \tag{9}$$

,

Anisotropy is used to characterize the scattering phenomenon.

One of the important characteristics for the eigenvalue–eigenvector decomposition is that the parameters are rotation invariant, and the parameters are constant for rotation about the radar line of sight. Table 2 shows a nine-zone segmentation scheme and represents scattering mechanisms on the H-$\bar{\alpha}$ plane.

Table 2. The H-$\bar{\alpha}$ Plane Partitioned into Nine Zones [2,7].

Zone	Entropy, H	Alpha, $\bar{\alpha}$ (°)	Scattering Type
1	0.9–1.0	55–90	High Entropy Multiple Scattering
2	0.9–1.0	40–55	High Entropy Vegetation Scattering
3	0.9–1.0	0–40	High Entropy Surface Scattering
4	0.5–0.9	50–90	Medium Entropy Multiple Scattering
5	0.5–0.9	40–50	Medium Entropy Vegetation Scattering
6	0.5–0.9	0–40	Medium Entropy Surface Scattering
7	0–0.5	47.5–90	Low Entropy Multiple Scattering Events
8	0–0.5	42.5–47.5	Low Entropy Dipole Scattering
9	0–0.5	0–42.5	Low Entropy Surface Scattering

4. Results and Discussion

4.1. Freeman–Durden Decomposition

Figure 3 shows ortho-rectified Freeman–Durden decomposition images with the double-bounce shown in red, volume scattering in green, and surface scattering in blue for the data obtained before the disaster on 19 May 2006 in descending orbit; after the disaster on 24 November 2008 in descending orbit; and on 4 June 2009 in ascending orbit. Volume scattering is dominant within the extensive areas of forest coverage.

Landslide areas upstream of Aratozawa Dam, Dozou-sawa, Ubusume-gawa, and Hiya-sawa on the post-earthquake image show a larger surface scattering component than that on the pre-earthquake image, and are consistent with the results derived by Watanabe *et al.* [10]. Surface scattering at the landslide areas east of Mt. Kurikoma, Ubusume-gawa, and Dozou-sawa are recognized in the post-earthquake images (see Figure 3(b,c,e–h)). Strong surface scattering upstream of Aratozawa Dam also appeared on the post-earthquake images Figure 3(b,c), but this area was beyond the observation area on 19 May 2006 (Figure 3(a)).

Strong surface scattering is found in the upper-left of Figure 3(a), in the area corresponding to the upper slopes of Mt. Kurikoma. The AVNIR-2 image for 21 May 2006 shows that this area was covered by snow, which may induce strong surface scattering. Some farmland in the middle of the target area shows dominant surface scattering. Table 3 shows the contribution of the scattering components derived from Freeman–Durden decomposition and double-bounce, volume, and surface scattering within the landslide areas denoted "A" (Dozou-sawa) and "B" (Ubusume-gawa), shown by the yellow rectangles in Figure 3(a–c). The images obtained of both areas on 19 May 2006, prior to the earthquake, show that volume scattering accounts for more than 81% and surface scattering represents 14%. On the other hand, three datasets from the descending orbit obtained after the earthquake show 63–67% for the volume scattering and 29–33% for the surface scattering components at these two landslide areas. After the earthquake, there was a shift of between 15 and 19%, from the volume scattering to surface scattering component. There are three possible causes for stronger volume scattering ratio in landslide areas.

(A) Volume scattering from fallen trees within the landslide areas. The presence of fallen trees within the landslide areas was confirmed by aerial photographs and field observations.

(B) Very rough surfaces induce a σ^0_{hv} component, leading to an erroneous volume scattering component.

(C) Small contribution from forest areas, even if the areas enclosed by the yellow rectangles in Figure 3 are occupied by the landslide areas.

Since the regions enclosed by the yellow rectangle are largely occupied by the landslide sites, and the values change between the pre- and post-disaster measurements, we regarded the values in Table 4 as representative of landslide areas.

Figure 3. Ortho-rectified Freeman–Durden decomposition images for (**a**) 19 May 2006, (**b**) 24 November 2008, and (**c**) 4 June 2009. White rectangle area with Dozou-sawa and Ubusume-gawa is expanded and shown in (**d**) 19 May 2006, (**e**) 24 August 2008, (**f**) 9 October 2008, (**g**) 24 November 2008, and (**h**) 4 June 2009. The image shows double-bounce scattering as red, volume scattering as green, and surface scattering as blue.

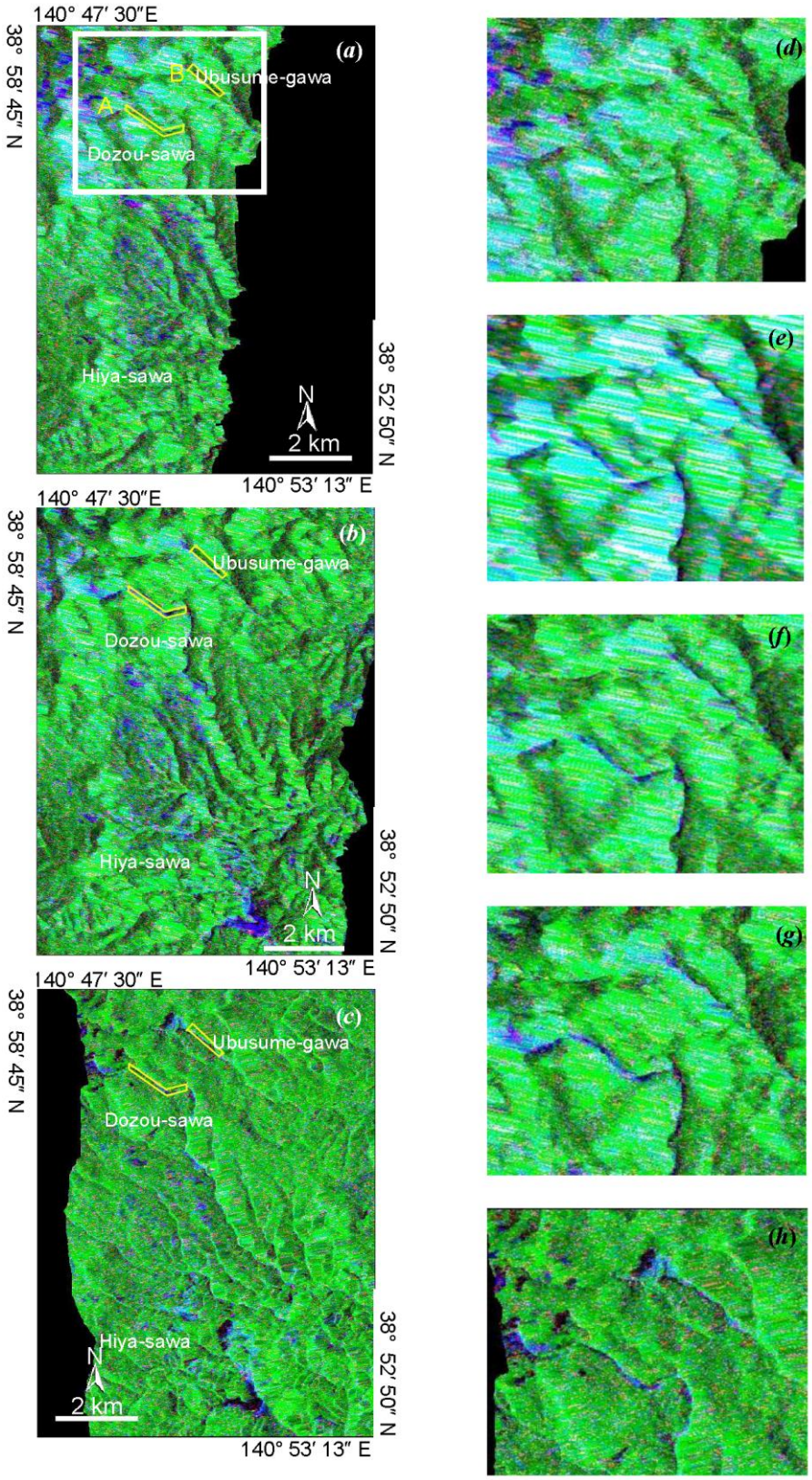

The data obtained on 4 June 2009 in the ascending orbit shows volume scattering at 69% and surface scattering at 25% in the Dozou-sawa area, and volume scattering at 79% and surface scattering at 17% in the Ubusume-gawa area. The surface scattering ratio in the Ubusume-gawa area in the ascending orbit image is smaller than that of the later image, obtained in descending orbit. The discrepancy between the ascending and descending observations is not outstanding for H-$\bar{\alpha}$ parameters shown in Table 4 of the next section, and no significant difference was observed for the land surface of the landslide areas. This is explained by the rotation invariance of H-$\bar{\alpha}$ parameters, which are robust to the difference in observation direction. The percentage of double-bounce scattering is 4–6% within both landslide areas on every image.

Table 3. Percentage of dominant scattering mechanism in areas associated with landslides following the 14 June 2008 Earthquake.

	A (Dozou–sawa)			B (Ubusume–gawa)		
(%)	***Pd***	***Pv***	***Ps***	***Pd***	***Pv***	***Ps***
19 May 2006	4.5	81.7	13.8	5.0	81.0	14.1
24 August 2008	3.7	63.5	32.8	4.6	66.9	28.6
9 October 2008	4.9	63.2	31.9	5.2	66.0	28.8
24 November 2008	4.1	65.9	30.0	4.3	67.0	28.7
4 June 2009	6.2	69.2	24.6	4.8	78.7	16.5

Pd: Double bounce scattering, *Pv*: Volume scattering, *Ps*: Surface scattering.

4.2. H / A / Alpha Decomposition

Figure 4 shows an H-$\bar{\alpha}$ classification map with range–azimuth projection. Entropy is lower over the landslide area than it is over the surrounding forest areas. Entropy comes from the randomness of the scattering process. High entropy is caused by the depolarizing effects of volume scatter from the structural elements of trees, which produce greater disorder in scattering. Alpha is high for forest areas and is low on bare surfaces, snow, and water surfaces. No significant differences were found in the anisotropy image. These results are consistent with those obtained by Czuchlewski *et al*. [7].

Table 4 shows the entropy and alpha values, averaged over 4 × 16 windows from forest, agricultural, landslide, water surface, and snowcapped areas, and the values are plotted in Figure 4(e). For comparison, the same area sizes are picked from each category. The window size of 4 × 16 ensures that pixels of the same category are included in a site. Since the width of the landslide areas is narrow, the window size is almost decided by the size of the landslide areas. Each set of windows is selected from every dataset, including the corresponding areas denoted on Figure 4 as "A" (forest), "B" (agricultural), "C" (landslide), "D" (landslide), "E" (landslide), "F" (snow), and "G" (snow). Every dataset shows a similar behavior, with relatively high entropy and alpha on the forest areas. The landslide areas show lower entropy and alpha than the forest areas. Polarimetric entropy is more than 0.7 for forest areas, compared with 0.52 to 0.63 for the landslide areas. The alpha angle for the forest areas is 47–52 and is 29–37 for the landslide areas. The agricultural areas show 0.59–0.70 for entropy and 30–40 for alpha, and these values are similar to those of the landslide areas. This finding implies that additional information, such as additional parameters [10] or pre-disaster land use classification, is required to identify the landslide areas. Snow surface on 19 May 2006 shows lower entropy (0.14–0.28) and alpha

(8–16) than the other land cover types. The entropy value of the water surface at Aratozawa Dam is 0.43–0.26, and is lower than that of the forest and the landslide areas. The relatively low entropy values correspond with the areas where surface scattering is dominant. The effect of different observation directions is evident from agricultural and water surface areas, and both the entropy and alpha values of ascending data are larger than those of the descending data for these areas. Ridges on agricultural fields and waves on the water surface may cause direction-dependent backscattering.

Figure 4. Unsupervised classification image using H-$\bar{\alpha}$ segmentation with eight looks in azimuth for (**a**) 19 May 2006, (**b**) 24 November 2008, and (**c**) 4 June 2009; (**d**) Partitioning and color legend, with numbers referring to the region described in Table 4; (**e**) H-$\bar{\alpha}$ plot for each area shown in Table 4.

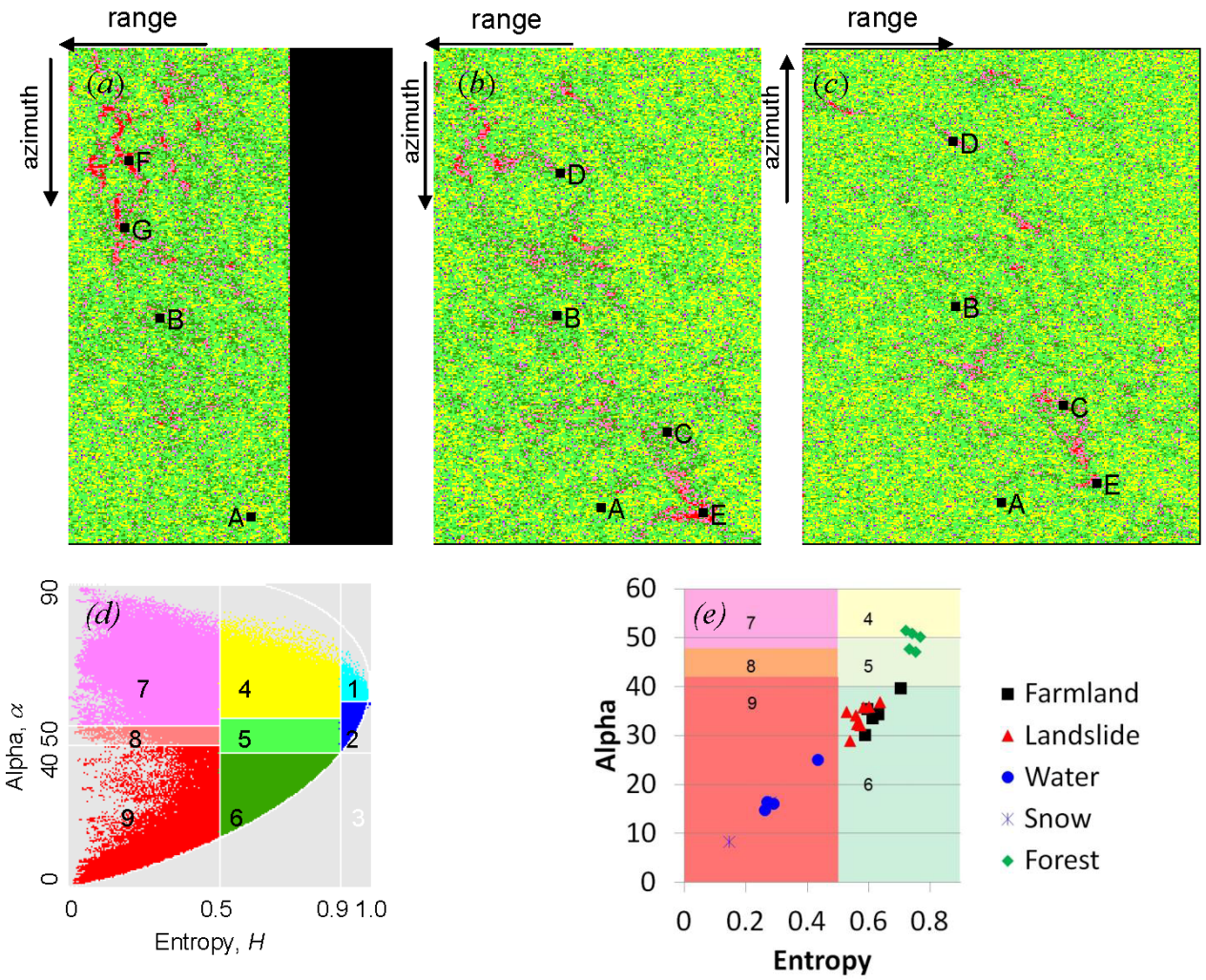

The H-$\bar{\alpha}$ classification space has nine zones according to scattering mechanisms (Table 2, Figure 4(d)). Large-scale landslide areas with bare surfaces are categorized as 6, 7, 8, and 9, whereas they were categorized as 5, 6, and 9 in a previous study [7]. The extension to high alpha angle (zones 7 and 8) is observed in our data, which we take as evidence for the mixture of fallen trees in the landslide area, as observed in the field. Forest areas are categorized as zones 4 and 5, whereas they were categorized as 5 in a previous study [7]. The discrepancy may be explained by differing forest types. Water surfaces show strong surface scattering areas. A large proportion of the water surface is classified as category 9, surrounded by category-6 areas. This is consistent with the airborne SAR

analysis [7], and explains that the water surface is smoother than the landslide surface on the scale of L-band radar wavelength. Snowcapped slopes on a 19 May 2006 image were also categorized as zone 9, and behave similarly to water surfaces. A previous analysis of dry Alpine snow using L-band SAR reported that surface backscattering was the major scattering mechanism at the snow–ground interface, and that volume scattering and extinction were small [18].

Table 4. Average of Entropy and Alpha Values of 4 × 16 Windows.

Area	Observation Date	Entropy	Alpha
Forest (A*)	19 May 2006	0.741	50.936
	24 August 2008	0.720	51.511
	9 October 2008	0.767	50.184
	24 November 2008	0.751	47.148
	4 June 2009	0.731	47.794
Farmland (B*)	19 May 2006	0.611	33.617
	24 August 2008	0.595	35.439
	9 October 2008	0.587	30.218
	24 November 2008	0.630	34.434
	4 June 2009	0.704	39.695
Landslide (C*)	24 August 2008	0.636	36.947
	9 October 2008	0.561	32.441
	24 November 2008	0.581	35.824
	4 June 2009	0.527	34.888
Landslide (D*)	24 August 2008	0.573	32.176
	9 October 2008	0.538	29.005
	24 November 2008	0.601	35.962
	4 June 2009	0.557	34.237
Water (E*)	24 August 2008	0.290	16.086
	9 October 2008	0.268	16.456
	24 November 2008	0.262	14.871
	4 June 2009	0.434	25.153
Snow (F*)	19 May 2006	0.145	8.337
Snow (G*)	19 May 2006	0.279	16.471

*Letters correspond to areas denoted in Figure 4.

4.3. Comparison with Single Polarization Observation

Figure 5(a) shows an image of Aratozawa Dam obtained by dividing an HH polarization intensity image observed on 23 June 2008 by one observed on 23 March 2008. These data were acquired on ascending orbit with a 34.3 ° incidence angle. Accumulations of black or white pixels indicate large changes of radio-filled intensity, and also reveal changes in topographic features. The bright (white) area denoted as "A" corresponds to sediments flowing into the reservoir. The low values (black) denoted as "B" show occurrences of radar shadow by topographic features that were changed by the earthquake. Formation of a cliff in this region by a landslide was confirmed by field survey after the earthquake (Figure 5(b)). This radar shadow area is found on the polarimetric Freeman–Durden decomposition image obtained from ascending orbit (Figure 3(c)). Descending images do not show

this radar shadow, and the resultant images of eigenvalue–eigenvector decomposition do not include the effect of the radar shadow.

Figure 5. (**a**) Single-polarization intensity image for Aratozawa Dam reservoir area observed on 23 March 2008, divided by the image from 23 June 2008; (**b**) On-site photograph taken around Area "B".

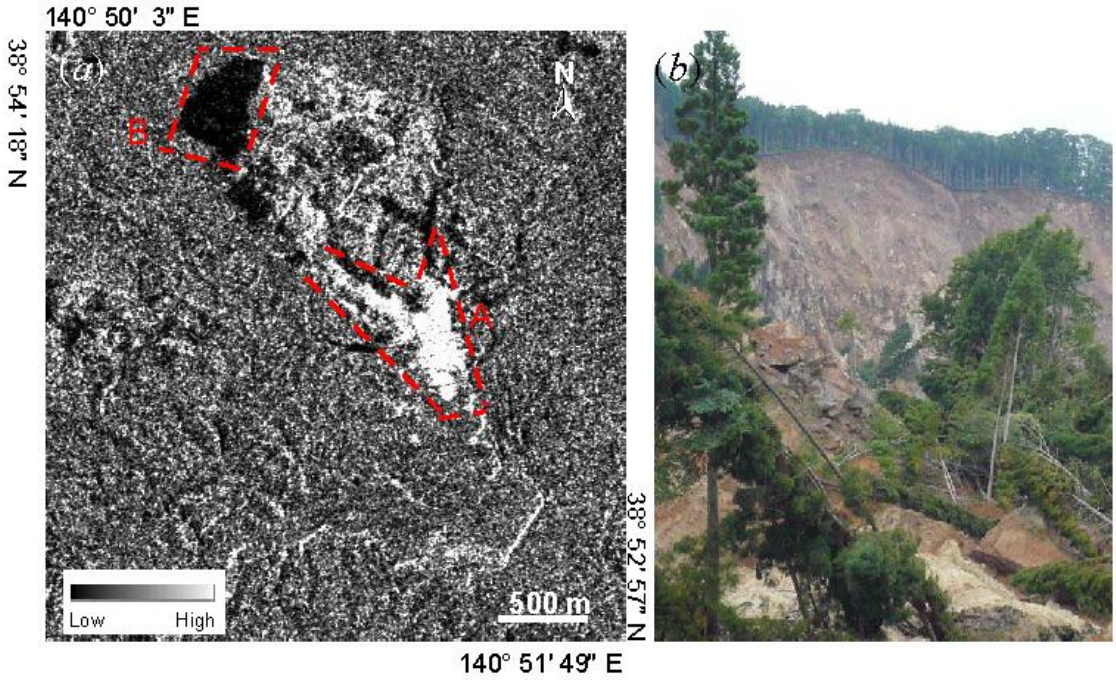

Yonezawa *et al.* [19] suggested that PALSAR single polarization data are useful to detect changes in terrain on landslides upstream of Aratozawa Dam and the temporal sequence of drawdown of the dammed lake. Single polarization data detects changes to land features, but a pre-landslide image is essential for the comparison. Spatial resolution of a full polarimetric image is coarser than that of a single polarization image. However, full polarimetric data can assess land surface coverage from the scattering mechanism. For example, the landslide at Ubusume-gawa is not recognized from visual interpretation of single polarization data; however, it is clearly extracted on the full polarimetric data obtained after the earthquake.

5. Conclusions

We employed Freeman–Durden decomposition and eigenvalue–eigenvector decomposition for ALOS (Advanced Land Observation Satellite) PALSAR (Phased Array type L-band Synthetic Aperture Radar) full polarimetric data. Data observed from different directions, ascending and descending orbit with small incidence angles (21.5° and 23.5°) were examined in this study. Land surface change from forest to bare soil due to landslides causes the scattering mechanism to change. The surface scattering component is dominant in landslide areas. The volume scattering component is strong in the forest areas. Agricultural, snow, and water surface areas also show a large surface scattering component compared to forest areas. Unsupervised classification using the H-$\bar{\alpha}$ plane makes it possible to distinguish landslide areas from water and snow surface areas. Snow coverage and water

areas generally show lower H and $\bar{\alpha}$ values compared to landslide areas. Agricultural areas show similar scattering characteristics to those of landslide areas. Areas of bare soil, that were present before the earthquake, should show the same scattering properties as the landslide area. The difference in the direction of geometric distortion associated with the differing observation direction has a slight effect on the scattering ratio, H, and $\bar{\alpha}$ values; however, the overall scattering properties are consistent with each other. We conclude that landslide areas are well recognized by the post-earthquake full polarimetry image, except for areas of farmland or bare soil. Classification accuracy is improved if the land coverage before the disaster is known from optical sensors, aerial photographs, or other references. Single polarization PALSAR images show landslide areas as topographic features that differ before and after the earthquake. However, single polarization data is unsuitable for efficient detection of landslide areas because of its difficulty in land cover classification.

Acknowledgments

ALOS data were provided under the agreement of a JAXA Research Announcement. We thank the ESA/PolSARpro project team for providing the analysis software free of charge. This work is supported by the Tohoku Construction Association and Japan Society for the Promotion of Science (JSPS) Grants-in-Aid for Scientific Research, (C) 24510252.

References

1. Boerner, W.M.; Mott, H.; Luneburg, E.; Livingstone, L.; Brisco, B.; Brown, R.J.; Paterson, S. Polarimetry in Remote Sensing: Basic and Applied Concepts. In *Principles and Applications of Imaging Radar*; Henderson, F.M., Lewis, A.J., Eds.; Wiley: New York, NY, USA, 1998; Chapter 5, pp. 271–357.
2. Cloude, S.R.; Pottier, E. An entropy based classification scheme for land applications of polarimetric SAR. *IEEE Trans. Geosci. Remote Sens.* **1997**, *35*, 68–78.
3. Freeman, A.; Durden, A.L. A three-component scattering model for polarimetric SAR data. *IEEE Trans. Geosci. Remote Sens.* **1998**, *36*, 963–973.
4. Yamaguchi, Y.; Yajima, Y.; Yamada, H. Four-component scattering model for polarimetric SAR image decomposition. *IEEE Trans. Geosci. Remote Sens.* **2005**, *43*, 1699–1706.
5. Cloude, S.R.; Pottier, E. A review of target decomposition theorems in radar polarimetry. *IEEE Trans. Geosci. Remote Sens*. **1996**, *34*, 498–518.
6. Alberga, V.; Satalino, G.; Staykova, D.K. Comparison of polarimetric SAR observables in terms of classification performance. *Int. J. Remote Sens.* **2008**, *29*, 4129–4150.
7. Czuchlewski, K.R.; Weissel, J.K.; Kim, Y. Polarimetric synthetic aperture radar study of the Tsaoling landslide generated by the 1999 Chi-Chi earthquake, Taiwan. *J. Geophys. Res.* **2003**, *108*, doi:10.1029/2003JF000037.
8. Rodriguez, K.M.; Weissel, J.K.; Kim, Y. Classification of Landslide Surfaces Using Fully Polarimetric SAR: Examples from Taiwan. In *Proceedings of 2002 IEEE International Geoscience and Remote Sensing Symposium*, Toronto, ON, Canada, 24–28 June 2002; pp. 2918–2920.
9. Watanabe, M.; Shimada, M.; Moriyama, T.; Tadono, T. An detectability of debris flow by using PALSAR and PiSAR (L-band) data (in Japanese). *J. Remote Sens. Soc. Jpn*. **2007**, *27*, 386–393.

10. Watanabe, M.; Yonezawa, C.; Iisaka, J.; Sato, M. ALOS/PALSAR full polarimetric observations of the Iwate-Miyagi Nairiku earthquake of 2008. *Int. J. Remote Sens*. **2012**, *33*, 1234–1245.
11. Ushiyama, M.; Ohta, Y. Characteristics of death or missing caused by the Iwate-Miyagi Nairiku Earthquake in 2008 (in Japanese). *J. Jpn. Soc. Natural Disaster Sci.* **2009**, *28*, 59–66.
12. Kisanuki, J.; Sekiguchi, T.; Sakai, H.; Nouguchi, T.; Tasaki, A. Responses of geographic department of GSI to the Iwate-Miyagi Nairiku earthquake in 2008 (in Japanese). *J. Geogr. Survey Instit*. **2008**, *117*, 49–58.
13. Ohno, H.; Ishii, H.; Nakajima, S.; Takahashi, S.; Watanabe, K. Photogrammetric analysis of landslides caused by the Iwate-Miyagi Nairiku earthquake in 2008 (in Japanese). *J. Geogr. Survey Instit*. **2008**, *117*, 39–47.
14. Sakurai, M.; Inagaki, H.; Ueno, S.; Goto, S. Characteristics of Land Slide Area with Long Distance of Flow Caused by 2008 Iwate-Miyagi Nairiku Earthquake in Northern Japan (in Japanese). In *Proceedings of the 23rd Conference of Japan Society of Erosion Control Engineering*, Hiroshima, Japan, 27–29 May 2009.
15. Pottier, E.; Ferro-Famil, L.; Allain, S.; Cloude, S.; Hajnsek, I.; Papathanassiou, K.; Moreira, A.; Williams, M.; Minchella, A.; Lavalle, M.; Desnos, Y.-L. Overview of the PolSARpro V4.0 Software. The Open Source Toolbox for Polarimetric and Interferometric Polarimetric SAR Data Processing. In *Proceedings of 2009 IEEE International Geoscience and Remote Sensing Symposium*, Capte Town, South Africa, 12–17 July 2009; pp. IV-936–IV-939.
16. Lee, J.S.; Grunes, M.R.; de Grandi, G. Polarimetric SAR Speckle filtering and its implication for classification. *IEEE Trans. Geosci. Remote Sens*. **1999**, *37*, 2363–2373.
17. Van Zyl, J.J. Unsupervised classification of scattering behavior using radar polarimetry data. *IEEE Trans. Geosci. Remote Sens.* **1989**, *27*, 36–45.
18. Shi, J.C.; Dozier, J. Estimation of snow water equivalence using SIR-C/X-SAR, Part I: Inferring snow density and subsurface properties. *IEEE Trans. Geosci. Remote Sens*. **2000**, *38*, 2465–2474.
19. Yonezawa, C.; Chiba, K.; Kato, T. Damage to agricultural land due to the Iwate-Miyagi Nairiku Earthquake in 2008 observed by advanced land observation satellite (ALOS) (in Japanese). *J. Jpn. Soc. Irrig. Drain. Rural Eng.* **2009**, *77*, 549–552.